

ARENA: Adaptive Risk-aware and Energy-efficient NAVigation for Multi-Objective 3D Infrastructure Inspection with a UAV

David-Alexandre Poissant^{1–2}, Alexis Lussier Desbiens¹, François Ferland², and Louis Petit^{1–2}

Abstract—Autonomous robotic inspection missions require balancing multiple conflicting objectives while navigating near costly obstacles. Current multi-objective path planning (MOPP) methods struggle to adapt to evolving risks like localization errors, weather, battery state, and communication issues. This letter presents an Adaptive Risk-aware and Energy-efficient NAVigation (ARENA) MOPP approach for UAVs in complex 3D environments. Our method enables online trajectory adaptation by optimizing safety, time, and energy using 4D NURBS representation and a genetic-based algorithm to generate the Pareto front. A novel risk-aware voting algorithm ensures adaptivity. Simulations and real-world tests demonstrate the planner’s ability to produce diverse, optimized trajectories covering 95% or more of the range defined by single-objective benchmarks and its ability to estimate power consumption with a mean error representing 14% of the full power range. The ARENA framework enhances UAV autonomy and reliability in critical, evolving 3D missions.

Index Terms—Motion and Path Planning, Autonomous Vehicle Navigation, Aerial Systems: Applications, Optimization and Optimal Control, Robust/Adaptive Control

I. INTRODUCTION

Uncrewed aerial vehicles (UAVs) are becoming crucial tools in various scenarios where human involvement can become too risky or incur high costs, such as search and rescue [1], surveillance [2], and inspection [3], [4]. Achieving autonomy in these scenarios heavily relies on the path planning module to generate safe and feasible trajectories. Numerous approaches have been proposed to find the shortest or safest path in a cluttered environment. For intricate tasks, such as infrastructure inspection, ensuring safe maneuvers involves considering multiple factors, prompting increased interest in multi-objective optimization (MOO) methods.

In many cases, optimizing multiple objectives for path planning results in various viable paths, representing the optimal Pareto front, the primary goal of MOO. To our knowledge, most Multi-Objective Path Planning (MOPP) methods include static terms like safety, time, smoothness, or others to find the optimal front [5]. Some research estimates risks using offline data, such as satellite imagery and building positions [6], but lacks dynamic adaptation to mission conditions.

This research was funded by Alliance grant number 2601-2600-703 and CRIAQ between Université de Sherbrooke, Hydro-Québec and DRONE VOLT®.

¹The authors are with the Createk Design Lab, University of Sherbrooke, Sherbrooke, J1K 2R1, Canada, [david-alexandre.poissant, louis.petit, alexis.lussier.desbiens]@usherbrooke.ca

²The authors are with the Intelligent Interactive Integrated Interdisciplinary Robot Lab (IntRoLab), University of Sherbrooke, Sherbrooke, J1K 2R1, Canada, françois.ferland@usherbrooke.ca

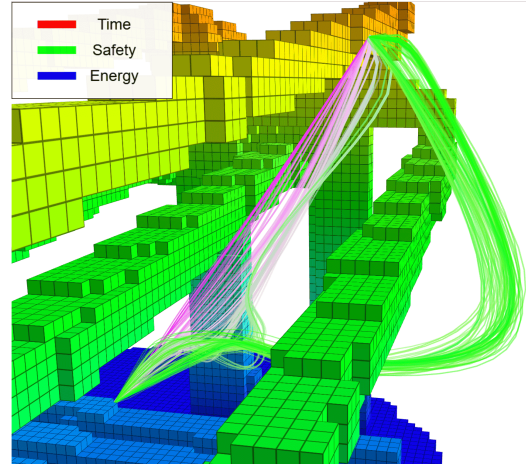


Fig. 1: Representation of every non-dominated trajectory at the end of ARENA’s process. An RGB model depicts the various objectives’ influence on a trajectory.

Our recent work introduced the Multi-Objective and Adaptive Risk-aware (MOAR) path planner [7], enabling real-time trajectory modulation by considering evolving risks. However, it relies on exhaustive graph searches in discretized 2D environments, limiting real-time applicability in large 3D spaces. In this letter, we propose an extended version of the MOAR path planner, broadening its use to 3D spaces and continuous representations. The proposed framework, named Adaptive Risk-aware and Energy-efficient Navigation (ARENA) MOPP, leverages a 4D Non-uniform rational B-spline (NURBS) [8] representation and the non-dominated sorting genetic algorithm (NSGA-II) [9] to compute feasible trajectories and modulate the velocity profile along them. It optimizes safety, time, and a novel energy objective while adapting to evolving risks like localization precision, wind, battery state, and communication. We show the reliability and efficiency of our framework in numerous simulations and real-world power line inspection scenarios. Although developed primarily for power line inspections, our method can be easily applied to different path planning problems in complex 3D environments, including most infrastructure inspection missions.

Section II reviews the state of the art on MOPP. Section III explains the fundamentals of MOO and NURBS to understand better our approach presented in Section IV. Section V shows the results of the sensitivity analysis and risk adaptability. We conclude this letter in Section VI by suggesting potential future works.

II. RELATED WORK

a) Multi-Objective Optimization and Risk Adaptivity:

MOPP methods are widely used for global trajectory generation in UAV applications, addressing various objectives [5]. A common approach to handling multiple objectives combines cost functions into a single scalar value. This typically involves weighing the objectives to obtain desirable behavior. In our previous work, we applied this method, integrating safety, energy, and time [7]. Similarly, the authors in [10] combined path length with a risk-utility function based on a risk map. Zhou et al. [11] introduced a gradient-based method that incorporates smoothness and feasibility functions to local graph search-based collision risks. While this approach simplifies the inherently multi-objective problems, the authors in [5] highlight several issues with this workflow. One key concern is that preferences between objectives may evolve over time and missions, making the transformation of an inherently multi-objective problem into a single cost function a semi-blind, manual process. Another approach to handling multiple objectives is proposed by the authors in [12] where they use A* independently on every objective to mimic specific behaviors and then use a voting algorithm to choose between them. While this method produces paths at the extreme edge of the Pareto front, it fails to address the key issue of evolving preferences between objectives over time, and does not allow for compromises that could better align with a specific situation.

b) *Risk Assessment:* Conducting a thorough risk assessment is essential to establish trust in UAV autonomous operations. Some studies introduce safety objectives to prevent unsafe trajectories during MOO processes. Ahmed et al. [13], [14] assess trajectory safety using the robot's range of vision. Many approaches maximize safety by minimizing collision risks with static or dynamic obstacles using clearance-based objectives [1]. Authors in [10] use collision risk maps, while [15] combines Gaussian processes and Evolutionary algorithms (EA) to map risks like signal strength and wind speed for single or multiple UAVs. However, these methods address fixed mission statements. As we highlighted in this section, preferences between objectives can shift dynamically during and between missions. Factors like worsening weather or GPS reception may prioritize safety, while battery constraints could favor faster or more energy-efficient paths. In our recent work, we introduced the concepts of damage cost in the event of a crash and non-insertion cost, which quantifies the degree of intrusion into important obstacle structures [7], providing situational awareness and a margin of error to respond effectively to dangerous situations.

c) *Trajectory Representation:* While not tied to a specific mission statement, our two concepts of damage and non-insertion costs are constrained to a 2D plane with discretely constructed paths, similar to [16], [17], leading to resolution loss and limited path optimality. To overcome this, [11] proposes B-spline parametrization to represent trajectories continuously, using knot vectors based on actuator limitations. However, this method lacks flexibility in modulating

trajectories. For instance, control points are positioned at fixed intervals, constraining the optimizer's ability to discover more optimal solutions. Another method, described in [18], proposes an n-dimensional NURBS approach that adds orientation components to XYZ control points. While this enables smoothing additional components of an Euclidean path, it relies on a look-ahead process to ensure compliance with actuator limitations. However, post-optimization adjustments undermine the optimization purpose, as they may deviate from the originally optimized solution.

d) *Energy Efficiency:* Energy efficiency is crucial for UAV missions, especially under battery constraints. Several methods exist to model energy consumption [19]. For example, [20] defines a detailed energy model for fixed-wing UAVs based on speeds and accelerations along trajectories. Other methods, like [21], empirically derive energy consumption by evaluating a drone under various scenarios to create situational equations. While validated through theoretical energy consumption, this approach depends on best-fitting curves rather than physics-based principles, making it scenario-dependent. To our knowledge, no method formulates a generalized data-driven energy model using physics-based principles.

In this paper, we introduce a novel framework for an online adaptive energy-efficient 3D multi-objective path planning algorithm designed to generate a Pareto set of trajectories that accommodate the risk variation during a mission. Our contributions are as follows: (a) we introduce a novel voting algorithm for choosing the best trajectory according to evolving mission risks, (b) we push further the notion of non-insertion cost introduced in our recent work [7], (c) we introduce a 4th dimension in a continuous representation tool to modulate and optimize speed while complying with actuator constraints, and (d) we present a novel semi-empirical energy consumption model that incorporates different flight situations.

III. FUNDAMENTALS

This section covers the essential concepts required to understand the algorithm described in Section IV. We begin by outlining the definition of a MOO process and conclude with an introduction to the trajectory representation tool utilized in our approach.

A. Multi-objective Optimization

The goal in MOO is to find a D -dimensional solution vector $z = [z_1 \dots z_D]^T$ that minimize or maximize a set \mathcal{F} of E objective functions

$$f_e(z), \quad e = 1, \dots, E \quad (1)$$

that can be subject to F inequality constraints

$$g_f(z) \geq 0, \quad f = 1, \dots, F \quad (2)$$

as well to G equality constraints

$$h_g(z) = 0, \quad g = 1, \dots, G \quad (3)$$

Additionally, each element of z can be limited by a lower and upper bound

$$z_d^{(L)} \leq z_d \leq z_d^{(U)}, \quad d = 1, \dots, D \quad (4)$$

The search space S contains all feasible solutions to the optimization problem. A solution is possible if it satisfies all constraints and bounds. Feasible solutions can be ranked by dominance, as no single solution may optimize all objectives simultaneously. A solution z_1 is said to dominate another solution z_2 ($z_1 \preceq z_2$) if z_1 is equal or better than z_2 for all objectives and strictly better in at least one. Each non-dominated solution forms the Pareto set.

B. Non-Uniform Rational B-Splines (NURBS)

A NURBS curve of order $p + 1$ is defined by Piegl et al. [8] as

$$C(u) = \frac{\sum_{i=0}^n N_{i,p}(u) w_i P_i}{\sum_{i=0}^n N_{i,p}(u) w_i} \quad (5)$$

where

- n is the number of control points,
- p is the degree of the basis function $N_{i,p}$,
- $P_i = [x_i \ y_i \ z_i]^T$ is the i^{th} control point (assuming a 3D curve), and
- w_i is its weight.

The basis functions $N_{i,p}$ are defined with respect to the parameter u and a fixed knot vector

$$U = [u_0 \ \dots \ u_m]^T \quad (6)$$

containing $m + 1$ knots, whereas $m = n + p$. The De-Boor-Cox formulas allow to calculate the basis function in recursion [8], [22], [23].

IV. ADAPTIVE RISK-AWARE PATH PLANNING

We begin this section by defining the multi-objective path planning problem. We present the decision vector, the continuous path representation method, and the objectives in Section IV-A. Section IV-B shows our adaptive risk-aware multi-objective path planning method, including our multi-objective solver and how we initialize it, the voting algorithm, the real-time adjustment of its coefficients, and the hyperparameters of the entire path planning method.

A. Problem Definition and Representation

We generalize the infrastructure inspection path planning scenario as a 4D problem, which we define as $\mathbb{D}^4 = \{(x, y, z, v) \mid x \in [x_{min}, x_{max}], y \in [y_{min}, y_{max}], z \in [z_{min}, z_{max}], v \in [-v_{max}, v_{max}]\}$ with start and goal positions $\{(x_a, y_a, z_a, v_a), (x_b, y_b, z_b, v_b)\} \in \mathbb{D}^4$. The goal of this MOPP problem is to find the NURBS curve $C = \{C(u) : u \in [a, b]\}$ that minimizes the set of objectives \mathcal{F} described below.

We choose to represent trajectories using NURBS [8], described in Section III-B, to benefit from their inherent properties for multidimensional multi-objective optimization.

These include *strong convex hull* properties, *local approximation* capability, and *infinite differentiability* apart from knot multiplicity [8]. The first two properties are helpful during optimization to constrain the curve inside a bounded area and to escape local minima by varying the curve locally. The last property ensures the smoothness of the curve according to the knot multiplicity of the curve, which is beneficial for UAVs that have strict actuator limitations, such as low acceleration. The design vector is given by:

$$z = [w_0 \ x_1 \ y_1 \ z_1 \ \|\vec{v}_1\| \ w_1 \ \dots \ x_{n-1} \ y_{n-1} \ z_{n-1} \ \|\vec{v}_{n-1}\| \ w_{n-1} \ w_n]^T \quad (7)$$

We introduce the 4th dimension to the parametric curve C , representing the velocity norm at each control point, enabling velocity profile modulation along trajectories as risks evolve. The start and goal positions, along with their speeds, are fixed and excluded from the decision vector z . The problem is constrained by two hard limits: acceleration (a_{max} in Table I) to meet actuator limitations and collision avoidance to ensure feasibility.

Costs are generalized into three functions to encompass multiple scenarios: time, safety, and energy consumption, which are described in the following subsections.

1) *Time cost*: The time cost is computed as:

$$\mathcal{F}_{Time} = \sum_{i=0}^{Q-1} \frac{d_i}{\|\vec{v}_{i+1}\|} \quad (8)$$

where Q is the number of sample points and d_i is the distance on the path segment. The $i + 1$ velocity is used, assuming inspection drones are slow and can quickly reach low speeds. Under normal conditions, with no significant risks during an inspection mission, the algorithm minimizes this cost function, prioritizing speeding up the inspection process over safety or energy consumption.

2) *Safety cost*: The safety cost consists of two terms:

$$\mathcal{F}_{Safety} = k_a \left(\frac{\sum_{i=0}^Q \mathcal{F}_{sdf_i}}{Q} + \max(\mathcal{F}_{sdf}) \right) + k_b \left(\frac{\sum_{i=0}^Q \mathcal{F}_{ch_i}}{Q} + \max(\mathcal{F}_{ch}) \right) \quad (9)$$

where \mathcal{F}_{sdf_i} is a collision cost to ensure a safe UAV-obstacle distance and \mathcal{F}_{ch_i} denotes a non-insertion cost for obstacles forming convex hulls to keep trajectories outside critical zones. In this letter, convex hulls, modeled as oriented bounding boxes (OBB), are dynamically adjusted around cables and pylons using semantic information during power line inspections. The coefficients k_a and k_b in Eq. 9 are normalized since \mathcal{F}_{sdf_i} and \mathcal{F}_{ch_i} return normalized values. Combining mean and maximum costs ensures overall trajectory safety while maximizing the minimum obstacle distance. To support this, we use a signed distance field (SDF) [24] alongside our path planning algorithm to maintain obstacle

information within the free space. \mathcal{F}_{sdf_i} is defined using the closest obstacle distance in the SDF:

$$\mathcal{F}_{sdf_i} = \begin{cases} 0 & d_{obs_i} \geq r_{sdf_{max}} \\ \frac{\lambda}{d_{obs_i}} - 1 & r_{sdf_{min}} < d_{obs_i} < r_{sdf_{max}} \\ 1 & d_{obs_i} \leq r_{sdf_{min}} \end{cases} \quad (10)$$

where $\lambda = \frac{r_{sdf_{min}} r_{sdf_{max}}}{r_{sdf_{max}} - r_{sdf_{min}}}$ is a scaling factor and d_{obs_i} is the distance between the UAV and the nearest obstacle. Both $r_{sdf_{min}}$ and $r_{sdf_{max}}$ are listed in Table I. This cost function reflects the increasing risks as the UAV gets closer to obstacles, which rapidly increases near them. The non-insertion cost function \mathcal{F}_{ch_i} is formulated as follows:

$$\mathcal{F}_{ch_i} = \sum_{i=0}^N \begin{cases} 0 & d_{ch_i} \geq r_{ch_{max}} \\ 1 - \frac{d_{ch_i}}{r_{ch_{max}}} & 0 < d_{ch_i} < r_{ch_{max}} \\ 1 & d_{ch_i} \leq 0 \end{cases} \quad (11)$$

where d_{ch_i} is the distance to the nearest convex hull and $r_{ch_{max}}$ is the maximum influence radius of convex hulls. Under high wind, communication, or localization risks, the algorithm prioritizes safety by selecting trajectories that minimize this cost function over time or energy efficiency.

3) *Energy cost*: To evaluate the energy consumption of a planned trajectory, our approach integrates physics-based principles with experimental data. [25] proposed a model for quadrotor UAVs with BLDC motors, showing that energy consumption varies with the flight state. According to this model, it can be hypothesized that for a given flight speed, horizontal movements require more power than hovering, with vertical movements further affecting it. The pitch/roll power relationship with the vertical axis forms a quadric surface [26], described by a general equation:

$$ax^2 + by^2 + cz^2 + dxy + eyz + fxz + gx + hy + kz + L = 0 \quad (12)$$

Because of a quadrotor's symmetry and to simplify the model, coupling terms are eliminated. The term L acts as a geometric translation factor and is fixed so the system doesn't return the trivial solution. With these simplifications, power data from minimally the six flight directions ($\pm Z, \pm Roll, \pm Pitch$) creates a solvable system of equations. To locate a point on this surface during optimization, we project along a unit vector $\hat{v} = (v_x, v_y, v_z)$, parameterized by t : $x = tv_x, y = tv_y, z = tv_z$. Substituting into Eq. 12 simplifies to:

$$At^2 + Bt + L = 0 \quad (13)$$

where $A = av_x^2 + bv_y^2 + cv_z^2$, $B = gv_x + hv_y + kv_z$, and $L = 1$. The roots of this equation, solved using the quadratic formula, determine the points on the quadric surface along the unit vector, providing steady-state power consumption $P(\hat{v})$ at these coordinates. The energy consumption cost function is given by:

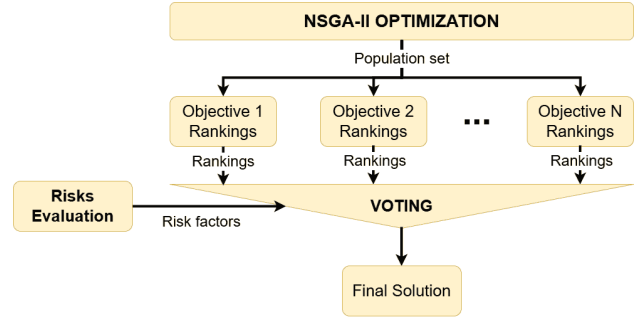


Fig. 2: Voting algorithm diagram

$$\mathcal{F}_{Energy} = \sum_{i=1}^Q P(\hat{v}_i) \Delta t \quad (14)$$

Since inspection drones are slow and quickly reach cruising speed, we assume steady-state flight energy consumption remains constant, with transient states contributing minimally. Unlike the time cost function, the energy cost function includes a directional factor influencing the optimizer. In low battery conditions, the algorithm prioritizes energy and time over safety.

B. Algorithm

Our adaptive risk-aware path planning algorithm has two steps. First, we use a multi-objective solver that returns a Pareto front of feasible trajectories. Then, we filter these trajectories with our voting algorithm to select the most suitable one based on real-time mission risks.

1) *Solver*: Among many multi-objective optimizers, we chose the NSGA-II genetic algorithm for its efficiency with continuous problems [9]. It uses polynomial mutation and simulated binary crossover to explore the search space. In its default implementation, NSGA-II initializes a population of μ individuals using a normal distribution within the bounded search space. However, due to hard constraints in our problem definition, at least one feasible trajectory must be in the initial population. We generate this trajectory using a rapidly exploring random tree algorithm named RRT-Rope [27], where equidistant path nodes serve as control points for the first decision vector as outlined in Eq. 7. A component-wise Gaussian filter $\mathcal{N}(z_i, \sigma^2 G)$ is applied to all decision variables except control point weights. We empirically set $\sigma^2 G = 15m$ for position variables and $\sigma^2 G = \frac{v_{max}}{2} m/s$ for velocity norms. All weights are set to $w_i = 1$. After optimizing the cost functions, the process yields a set of feasible solutions on a Pareto frontier.

2) *Voting*: We implemented a voting algorithm to select the best trajectory based on real-time risks (Fig. 2). Trajectories from the Pareto set are ranked according to the objectives, and using risk coefficients, the algorithm selects the most suitable solution. We leverage the plurality of optimized solutions to choose the one that best fits the current mission status. The voting behavior is given by:

$$R_{i_{Final}} = k_T R_{i_T} + k_S R_{i_S} + k_E R_{i_E} \quad (15)$$

where $R_{i_{Final}}$ is the final ranking of a solution and R_{i_T} , R_{i_S} , and R_{i_E} are the rankings of the solution's objectives compared to others in the Pareto set. The ranks coefficients k_T , k_S , and k_E are defined by our 4 mission risks: (a) wind risk \mathcal{WR} , (b) communication risk \mathcal{CR} , (c) localization risk \mathcal{LR} , and (d) battery risk \mathcal{BR} . These risks are estimated in real-time during the mission, based on factors like wind speed, motor saturation, data transmission speed, GPS satellite availability, dilution of precision, battery level, and return-to-home distance. As mentioned in [7], these coefficients can be adapted for other applications.

$$\begin{aligned} k_S &= \gamma k_{S,0} \left(1 + \left(\frac{1}{2}\mathcal{WR} + \frac{1}{4}\mathcal{CR} + \frac{1}{4}\mathcal{LR} - \mathcal{BR}\right)\right), \\ k_T &= \gamma k_{T,0} \left(1 - \left(\frac{1}{2}\mathcal{WR} + \frac{1}{4}\mathcal{CR} + \frac{1}{4}\mathcal{LR} - \mathcal{BR}\right)\right), \\ k_E &= \gamma k_{E,0} \left(1 + \left(\frac{1}{2}\mathcal{WR} + \frac{1}{2}\mathcal{BR}\right)\right), \\ 1 &= k_S + k_T + k_E \end{aligned} \quad (16)$$

Here, γ serves as a scaling factor for normalization. Adjusting the risks in real-time to modify an objective's influence addresses a key challenge in multi-objective optimization highlighted in [5].

3) *Hyperparameters*: In table I we give an overview of the most important hyperparameters of our path planning method. Note that the NSGA-II algorithm's crossover and mutation parameters were chosen according to the recommendation of the Pagmo library's NSGA-II implementation [28].

TABLE I: Hyperparameters for every step of our Adaptive Risk-Aware path planning method

	Parameter	Symbol	Value
General	UAV mass (kg)	m_{uav}	$\mathbb{R}_{>0}$
	UAV speed (m/s)	v_{max}	\mathbb{R}
	UAV acceleration (m/s ²)	a_{max}	\mathbb{R}
	NURBS curve degree	p	$\{x \in \mathbb{N} \mid 1 < x \leq 5\}$
	SDF influence radius	$[r_{sdf_{min}}, r_{sdf_{max}}]$	$\mathbb{N}_{>0}$
	Convex hull influence radius	$r_{ch_{max}}$	$\mathbb{N}_{>0}$
Algorithm step	Parameter	Symbol	Value
Initialization	RRT-Rope node distance	δ_{rope}	$\mathbb{R}_{>0}$
NSGA-II	Number of generations	N_{gen}	$\mathbb{N}_{>0}$
	Population size	N_{pop}	$\mathbb{N}_{>0}$
	Number of NURBS points	N_{nurbs}	$\mathbb{N}_{>0}$
Voting algorithm	Time coefficient	k_t	$\{x \in \mathbb{R} \mid 0 \leq x \leq 1\}$
	Safety coefficient	k_s	$\{x \in \mathbb{R} \mid 0 \leq x \leq 1\}$
	Energy coefficient	k_e	$\{x \in \mathbb{R} \mid 0 \leq x \leq 1\}$

V. RESULTS

We begin this section by presenting the experiment setup for simulated and real-world flight tests. Section V-B details our algorithm's performance compared to single-objective optimal behaviors through a parametric sensitivity analysis of the cost function coefficients. In Section V-C we discuss

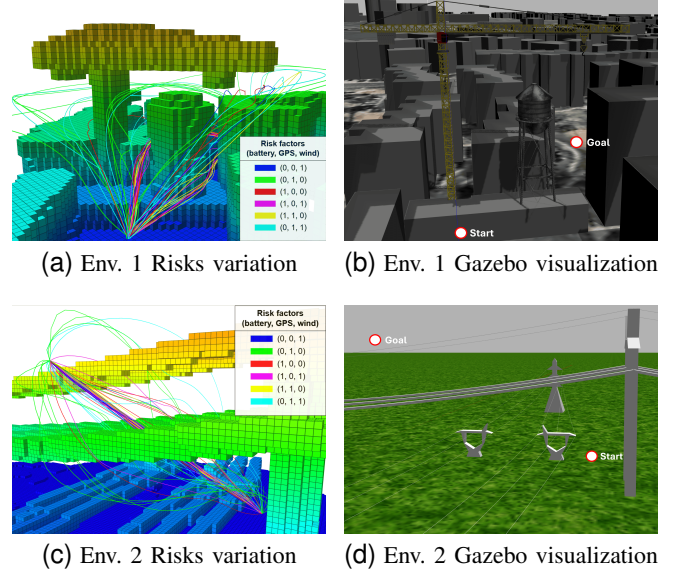


Fig. 3: Path comparison and Gazebo visualization: (a)-(c) Path comparison for different risk sets, with an RGB model indicating the risk influencing trajectory selection: red for low battery, green for localization, and blue for high wind risk. Obstacles are shown using an Octomap. (b)-(d) Gazebo simulations of a construction site and power lines model.

the algorithm's adaptability to different risk scenarios. Finally, overall behavior in real-world flight tests and power consumption model validations are presented and discussed in Section V-D.

A. Experiments Setup

The framework proposed in this paper is applied to a power line inspection problem [29], [30], using the Line-Drone robot [31], [32]. This UAV was developed by Hydro-Québec and DroneVolt to conduct in-contact non-destructive inspections on energized high voltage power lines. It has a GPS with a dual antenna for localization and orientation, a vertically mounted LiDAR for obstacle detection, and a Jetson Xavier NX to handle the computational load. The algorithm is implemented in C++11 and deployed using the Robot Operating System (ROS). We use different libraries, including the Open Motion Planning Library (OMPL) [33] for the initial trajectory conditions, Octomap [34] for obstacle detection, the Flexible Collision Library (FCL) [35] for collision detection on the initial trajectory, and Pagmo2 [28] for multi-objective optimization. Simulations were performed with a 2.3GHz i7 CPU running an 8-core processor and 16 GB RAM. The simulated drone mirrored the perception and localization capabilities of the LineDrone.

B. Simulated experiments

The approach was tested in 7 Gazebo environments: five reconstructed high voltage power lines environment, simulating power line inspections, and two industrial construction site scenarios with variations in the drone's position. This

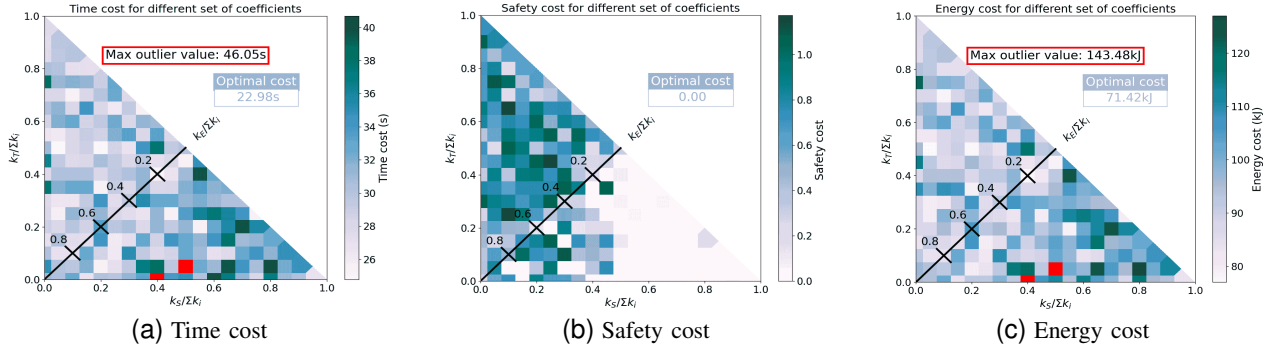


Fig. 4: Sensitivity study of the voting algorithm. The hyperparameters are set as follows: $v_{max} = 2.0$, $a_{max} = 2.2$, $p = 3$, $r_{sdf_{min}} = 1$, $r_{sdf_{max}} = 5$, $r_{ch_{max}} = 2$, $\delta_{rope} = 5.0$, $N_{gen} = 1000$, $N_{pop} = 40$, $N_{nurbs} = 50$. Every coefficients set is evaluated over 3 iterations.

paper highlights two of these environments, each presenting unique challenges, such as a wide-open search space or multiple trade-offs between safety, time efficiency, and energy efficiency.

The trajectories, shown in Fig. 3a, illustrate distinct behaviors: (a) red trajectories are faster but offer less obstacle clearance when battery risk is high, (b) green and cyan trajectories maintain greater distances from obstacles when wind and/or GPS risks are high, (c), blue trajectories save energy while maintaining minimum distance with obstacles, (d) intermediate behaviors arise from varying risk combinations.

The execution time of our algorithm depends on several hyperparameters. For our application, we found that $\delta_{rope} = 5.0$, $N_{gen} = 1000$, $N_{pop} = 40$, and $N_{nurbs} = 50$ with a NURBS curve degree of 3 consistently provide satisfactory results within 2 seconds on the simulation setup. The introduction of a 4th dimension to the NURBS makes δ_{rope} the most influential hyperparameter, as it controls the number of control points in the decision vector, affecting the size of the search space.

To benchmark our algorithm’s performance, we converted the multi-objective problem into a single objective one for each criterion. The algorithm was run ($\delta_{rope} = 2.0$, $N_{gen} = 2500$, $N_{pop} = 200$, $N_{nurbs} = 50$) 1000 times in each environment for each objective in every environment. We selected the minimum value for each criterion demonstrating specific behaviors in each environment: the fastest, the most energy-efficient, and the safest.

Fig. 4 illustrates a sensitivity analysis of our voting algorithm conducted in Env. 1 (Fig. 3b). We use the three cost functions to assess the algorithm’s response to varying mission risks. The coefficients are normalized and summed to one, ensuring only their relative values influence the objective rankings. This normalization allows representation on a 2D plane, with the k_E axis at 45 degrees. Outliers above 3σ are marked in red, and the maximum value is indicated. The results show that the algorithm consistently produces a Pareto frontier across a broad range of objective values. Increasing a coefficient reduces its associated cost: higher safety coefficients yield safer trajectories, while higher time

and energy coefficients lead to faster, more energy-efficient ones. The safety objective shows more distinct minima, while energy and time costs display smoother transitions, indicating greater sensitivity to weight adjustments for these objectives. This supports dynamic trade-offs as risks change. Our algorithm achieves optimal safety-focused solutions and produces fast and energy-efficient solutions that deviate only 7.8% and 7.9%, respectively, from the benchmarks. These results demonstrate the algorithm’s robustness and capacity to yield near-optimal solutions even with moderate hyperparameter adjustments.

C. Risk Adaptability

Fig. 5 shows the average distance to obstacles, path duration, and total energy consumption for Pareto front trajectories, analyzed as functions of three mission risks: battery, wind, and GPS. These risks were varied from 0 to 1 in 0.1 increments in Env.2 to isolate sensitivity to each risk. Communication risk was excluded as it mirrors localization risk in Eq. 16. Results indicate that with high battery risk, the planner prioritizes trajectories with path duration and energy consumption closest to benchmarks. With wind or localization risks, it prioritizes trajectories with obstacle distances closest to the safety benchmark. The planner’s trajectories span the full benchmark range for path duration and energy consumption, and 95.6% for obstacle distance. Similar results across seven environments confirmed the algorithm’s adaptive weighting based on varying risks.

D. Physical Experiments

The feasibility of our approach was validated through real-world flight tests with the LineDrone in a scaffold structure mimicking a power line inspection mission. Fig. 6 shows the results, where the UAV followed two trajectories: one optimized for energy efficiency, passing between structures to reach its goal faster, and another optimized for safety, with a larger average safety distance to obstacles. The computation times on the LineDrone’s computer were slightly over 4 seconds, using the recommended hyperparameter values. The results demonstrate the algorithm’s ability to plan behaviors tailored

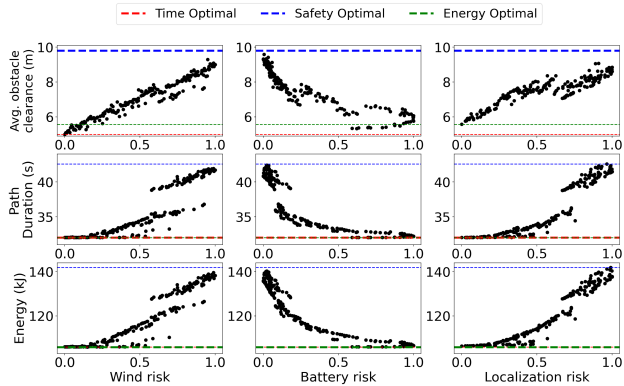


Fig. 5: Metric sensitivity to risk factors: average distance to obstacles, path duration, and energy consumption.

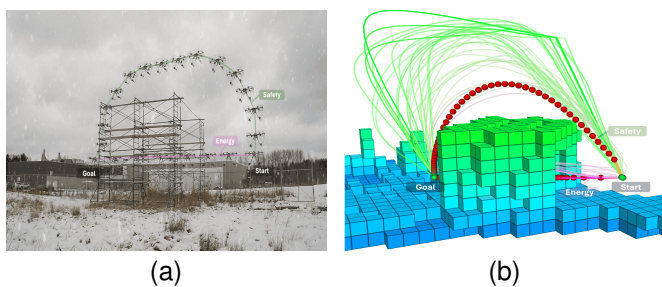


Fig. 6: Flight test with the LineDrone on a power line model. (a) Path reconstructed from a video. (b) Planned Pareto front. Safety trajectory has coefficients $k_s = 0.5$, $k_t = 0.1$, and $k_e = 0.4$. Energy trajectory has coefficients $k_s = 0.05$, $k_t = 0.05$, and $k_e = 0.9$. For simplicity, no non-insertion zone was defined, allowing the optimizer to plan trajectories going over the infrastructure.

to specific risk scenarios, prioritizing either energy savings or obstacle clearance.

To construct and validate our power consumption model, we conducted 42 real-world flight tests, where the UAV flew in 42 different directions at a speed of 2 m/s for 14 seconds to capture steady-state power consumption. We used data from the six directional axes (14% of the dataset) to construct the model, reserving the remaining 86% for validation. Fig. 7a illustrates model performance with a Bland-Altman plot, where the six data points used for model construction are marked with vertical lines and excluded from evaluation. The blue shaded area corresponds to pitch and roll maneuvers with descent, while the green shaded area represents pitch and roll maneuvers involving ascent. The results show good agreement between our model and the dataset, with the model’s validation dataset yielding a mean error of $11\text{W} \pm 118\text{W}$ corresponding to 0.97% of the full power range (1137.6W). We also applied the model to real-world flight trajectories, as shown in Fig. 7b and Fig. 7c. The estimations returned by our model closely follow the real power consumption trends observed during flights. For the safest trajectory, the model’s absolute mean error

was 160.9W (14% of the full power range), and for the energy-efficient trajectory, the error was 74.7W (6.6% of the same range). Transient effects did not induce noticeable power peaks, confirming our initial hypothesis. These results show that our model is sufficiently accurate to estimate power consumption, enabling the optimizer to generate more energy-efficient trajectories.

VI. CONCLUSION

In this paper, we investigate the MOPP problem of inspection missions with a UAV. We propose a novel approach, combining risk-awareness through a voting algorithm and a genetic optimizer, a 4D continuous trajectory representation tool, an energy consumption model, and coefficient adjustment to dynamically adapt to changing risk factors and transition smoothly between different planning behaviors. Our contributions to the field of MOPP are as follows: (a) we introduce a novel voting algorithm for choosing the best trajectory according to evolving mission risks, (b) we push further the notion of insertion cost introduced in our recent work [6], (c) we introduced a 4th dimension in a continuous representation tool to modulate and optimize speed while complying with actuator constraints, and (d) we present a novel semi-empirical energy consumption model that incorporates different flight situations.

The results highlight the effectiveness of our adaptive MOPP framework in generating diverse and near-optimal trajectories for inspection scenarios. Through simulated and real-world experiments, our algorithm proved its ability to adapt to varying risks, balancing safety, energy efficiency, and execution time spanning a broad range of evaluation metrics. Specifically, it covered 63% and 80% of the range defined by our behavioral benchmarks for path duration and average obstacle distance, respectively. Moreover, our energy consumption model successfully estimated real-world flight test trajectories with a 14% error at its worst. However, our method has limitations. Its computing time may be too high for applications requiring frequent replanning. Additionally, the energy consumption model assumes a steady-state regime and does not account for transient dynamics, limiting its applicability to UAVs where transient effects are significant.

In future studies, we aim to extend our energy consumption model to accommodate transient dynamics, thereby extending its use to more dynamic UAVs. We also plan to explore deep learning techniques to accelerate inference. Lastly, we intend to generalize our framework for other robotic platforms, such as ground and nautical systems, to demonstrate its versatility across a broad range of applications.

ACKNOWLEDGMENTS

The authors would like to thank Hydro-Québec and DRONE VOLT® for supplying the LineDrone. The authors also thank Sophie Stratford and Marc-Antoine Leclerc for their help during outdoor flights.

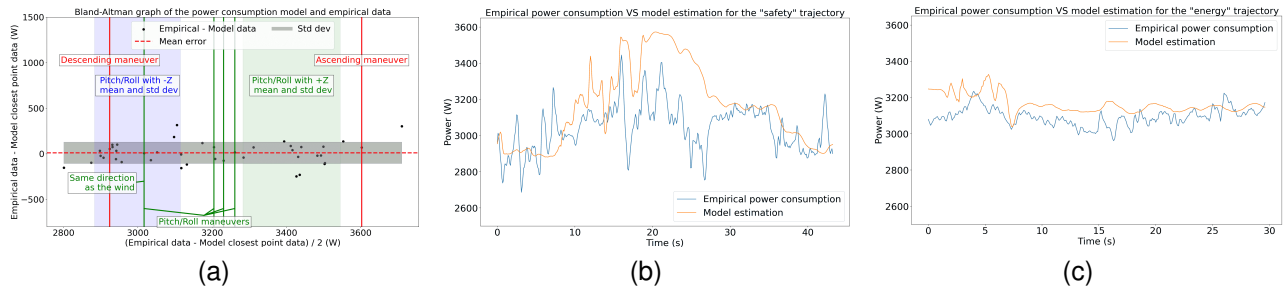


Fig. 7: Empirical power consumption data of a flight test with the LineDrone in windy conditions. (a) Bland-Altman graph of the empirical data VS the power model consumption's best fitting model (b)-(c) Model estimation VS real power consumption for the "safety" and "energy" trajectories in Fig. 6

REFERENCES

- [1] M. T. R. Khan, *et al.*, "Aspects of unmanned aerial vehicles path planning: Overview and applications," *International Journal of Communication Systems*, vol. 34, no. 10, Apr. 2021.
- [2] H. Shakhathreh, *et al.*, "Unmanned aerial vehicles (UAVs): A survey on civil applications and key research challenges," *IEEE Access*, vol. 7, pp. 48 572–48 634, 2019.
- [3] M.-A. Leclerc, *et al.*, "Netherdrone: a tethered and ducted propulsion multirotor drone for complex underground mining stope inspections," *Drone Systems and Applications*, vol. 11, pp. 1–17, 2023.
- [4] L. Petit and A. L. Desbiens, "Tape: Tether-aware path planning for autonomous exploration of unknown 3d cavities using a tangle-compatible tethered aerial robot," *IEEE Robotics and Automation Letters*, vol. 7, no. 4, pp. 10 550–10 557, 2022.
- [5] C. F. Hayes, *et al.*, "A practical guide to multi-objective reinforcement learning and planning," *Auton. Agent. Multi. Agent. Syst.*, vol. 36, no. 1, Apr. 2022.
- [6] F. Causa and G. Fasano, "Multi-objective modular strategic planning framework for low altitude missions within the urban air mobility ecosystem," *IEEE Transactions on Aerospace and Electronic Systems*, pp. 1–16, 2023.
- [7] L. Petit and A. Desbiens, "Moar planner: Multi-objective and adaptive risk-aware path planning for infrastructure inspection with a uav," in *IEEE International Conference on Robotics and Automation (ICRA)*, Yokohama, Japan, 2024.
- [8] L. Piegl and W. Tiller, *The NURBS book*. Berlin, Heidelberg: Springer-Verlag, 1995.
- [9] K. Deb, *et al.*, "A fast and elitist multiobjective genetic algorithm: Nsga-ii," *IEEE Transactions on Evolutionary Computation*, vol. 6, no. 2, pp. 182–197, 2002.
- [10] B. Weiss, M. Naderhirn, and L. del Re, "Global real-time path planning for UAVs in uncertain environment," in *IEEE Conference on Computer Aided Control System Design*, 2006, pp. 2725–2730.
- [11] X. Zhou, *et al.*, "EGO-planner: An ESDF-free gradient-based local planner for quadrotors," *IEEE Robotics and Automation Letters*, vol. 6, no. 2, pp. 478–485, 2021.
- [12] R. Korpan, "VBMO: Voting-based multi-objective path planning," 2023.
- [13] F. Ahmed and K. Deb, "Multi-objective path planning using spline representation," in *2011 IEEE International Conference on Robotics and Biomimetics*, 2011, pp. 1047–1052.
- [14] F. Ahmed and K. Deb, "Multi-objective optimal path planning using elitist non-dominated sorting genetic algorithms," *Soft Computing*, vol. 17, no. 7, pp. 1283–1299, Jul 2013.
- [15] J. Rubio-Hervas, A. Gupta, and Y.-S. Ong, "Data-driven risk assessment and multicriteria optimization of uav operations," *Aerospace Science and Technology*, vol. 77, pp. 510–523, 2018.
- [16] J. Song, S. Gupta, and T. A. Wettergren, "T*: Time-optimal risk-aware motion planning for curvature-constrained vehicles," *IEEE Robotics and Automation Letters*, vol. 4, no. 1, pp. 33–40, 2019.
- [17] S. Primatesta, G. Guglieri, and A. Rizzo, "A risk-aware path planning strategy for UAVs in urban environments," *J. Intell. Robot. Syst.*, vol. 95, no. 2, pp. 629–643, Aug. 2019.
- [18] R. M. Cheatham, W. E. Red, and C. G. Jensen, "Direct process control using n-dimensional NURBS curves," *Comput. Aided Des. Appl.*, vol. 2, no. 6, pp. 825–834, Jan. 2005.
- [19] J. Zhang, *et al.*, "Energy consumption models for delivery drones: A comparison and assessment," *Transportation Research Part D: Transport and Environment*, vol. 90, p. 102668, 2021.
- [20] Y. Zeng and R. Zhang, "Energy-efficient UAV communication with trajectory optimization," *IEEE Transactions on Wireless Communications*, vol. 16, no. 6, pp. 3747–3760, 2017.
- [21] H. V. Abeywickrama, *et al.*, "Comprehensive energy consumption model for unmanned aerial vehicles, based on empirical studies of battery performance," *IEEE Access*, vol. 6, pp. 58 383–58 394, 2018.
- [22] C. de Boor, "On calculating with B-splines," *Journal of Approximation Theory*, vol. 6, no. 1, pp. 50–62, 1972.
- [23] C. de Boor, *A Practical Guide to Splines*. New York: Springer-New York, 1978.
- [24] M. Jones, J. Baerentzen, and M. Sramek, "3d distance fields: a survey of techniques and applications," *IEEE Transactions on Visualization and Computer Graphics*, vol. 12, no. 4, pp. 581–599, 2006.
- [25] G. Jia, C. Li, and M. Li, "Energy-efficient trajectory planning for smart sensing in IoT networks using quadrotor uavs," *Sensors*, vol. 22, no. 22, 2022.
- [26] D. Hilbert and S. Cohn-Vossen, *Geometry and the Imagination*, ser. AMS Chelsea Publishing Series. AMS Chelsea Pub., 1999.
- [27] L. Petit and A. L. Desbiens, "RRR-Rope: A deterministic shortening approach for fast near-optimal path planning in large-scale uncluttered 3d environments," in *IEEE International Conference on Systems, Man, and Cybernetics (SMC)*, 2021, pp. 1111–1118.
- [28] F. Biscani and D. Izzo, "A parallel global multiobjective framework for optimization: Pagmo," *Journal of Open Source Software*, vol. 5, no. 53, p. 2338, 2020.
- [29] W. Chang, *et al.*, "Development of a power line inspection robot with hybrid operation modes," in *2017 IEEE/RSJ International Conference on Intelligent Robots and Systems (IROS)*, 2017, pp. 973–978.
- [30] J. Park, *et al.*, "Method of operating a gis-based autopilot drone to inspect ultrahigh voltage power lines and its field tests," *Journal of Field Robotics*, vol. 37, 10 2019.
- [31] F. Mirallès, *et al.*, "LineDrone technology: Landing an unmanned aerial vehicle on a power line," in *2018 IEEE International Conference on Robotics and Automation (ICRA)*, 2018, pp. 6545–6552.
- [32] P. Hamelin, *et al.*, "Discrete-time control of LineDrone: An assisted tracking and landing uav for live power line inspection and maintenance," in *2019 International Conference on Unmanned Aircraft Systems (ICUAS)*, 2019, pp. 292–298.
- [33] I. A. Şucan, M. Moll, and L. E. Kavraki, "The Open Motion Planning Library," *IEEE Robotics & Automation Magazine*, vol. 19, no. 4, pp. 72–82, December 2012, <https://ompl.kavrakilab.org>.
- [34] A. Hornung, *et al.*, "OctoMap: An efficient probabilistic 3D mapping framework based on octrees," *Autonomous Robots*, 2013, software available at <https://octomap.github.io>.
- [35] J. Pan, S. Chitta, and D. Manocha, "FCL: A general purpose library for collision and proximity queries," in *2012 IEEE International Conference on Robotics and Automation*, 2012, pp. 3859–3866.